ELSEVIER

Tectonophysics 247 (1995) 145–156

TECTONOPHYSICS

Drag along faults

Ze'ev Reches, Amir Eidelman [1]

School of Geology and Geophysics, University of Oklahoma, Norman, OK 73019, USA

Received 21 April 1994; revised version accepted 1 September 1994

Abstract

The bending of lines in the proximity of faults, known as fault-drag, is examined here by analytical and numerical (finite-element) models. Frequently, the bent lines are convex toward the direction of the fault motion, and this convexity is known as 'normal-drag', whereas an inverted sense of convexity is known as 'reverse-drag'. We first analyze the slip along a short fault embedded in a large elastic or elastic–plastic plate. The analysis indicates that reverse-drag is the expected drag along the short fault. Models with faults of high friction coefficient display smaller drag than frictionless faults; this suggests that the drag intensity is not simply related to the frictional resistance. We also model the drag along a normal fault with curved, 'anti-listric' surface embedded in an elastic–plastic medium; this model also indicates that the reverse-drag is the prevailing one. The predictions of the present models agree well with previous experimental results of slip along short faults in wax and plasticene samples. The normal-drag observed in association with long faults reflects prefaulting deformation which is concentrated within a narrow shear zone.

1. Introduction

The bending of layers and the curvature of igneous contacts at the proximity of faults is usually termed *fault drag*. The bent layers and the curved contacts are usually convex toward the direction of the block motion, and this convexity may be used to ascertain the sense of slip along faults (Fig. 1A) (Davis, 1984). In some cases however, the sense of convexity is inverted and this feature is known as *reverse drag* (Fig. 1B) (Hamblin, 1965). In this paper we examine the mechanisms of the development of fault drag and the origin of reverse drag.

A common notion is that fault drag forms due to the frictional resistance along the fault that is expected to partly restrain the slip along the fault (e.g., Hills, 1963; Billings, 1972). Thus, the displacement at the fault surface is smaller than the total displacement between the faulted blocks. The difference between the block displacement and the fault displacement is accommodated by the continuous deformation within the blocks; this deformation is the fault drag. Lines and layers that deform in this style are convex toward the direction of block motion (normal drag). A contrasting notion was raised by Dennis (1972, p. 302) who stated that " 'drag' features along faults

[1] Current address: Department of Geology, Hebrew University, Jerusalem 91904, Israel.

SSDI 0040-1951(94)00170-7

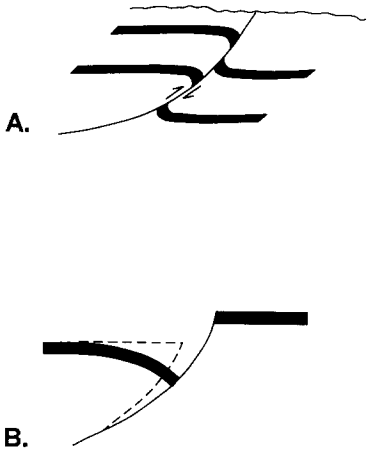

Fig. 1. Drag at the proximity of a fault. (A) Drag of layers close to a reverse fault. (B) Reverse drag or roll-over anticline along a listric normal fault (after Hamblin, 1965).

are probably not due to fault drag, but are evidence of ductile deformation which proceeded faulting."

Johnson (1970, ch. 3) suggested that fault drag is the local bending of layers at the proximity of the fault due to a combined effect of compression parallel to the layers and shear parallel to the fault. He showed that the shear stress along the fault surface amplifies the flexing of the layers at the immediate proximity of the fault. The amplitude of the drag fold is negligible at a distance of approximately half wavelength away from the fault.

Hamblin (1965) reviewed the processes of reverse dragging along normal faults and listed several possible mechanisms including multiple stages of deformation, elastic rebound, sagging, inversion of slip directions and differential compaction. He argued that as reverse drag is closely linked to normal faulting, it must be related to the geometry of normal faults. Hamblin (1965) attributed the reverse drag to the listric geometry of the faults that generates an additional volume in the upper part of the fault due to the slip along the deeper parts of the fault that dip gently (Fig. 1B). The collapse and bending of the hanging block into this additional space form the reverse drag, also know as roll-over anticline.

In the present study we examine the process of drag along faults for three simple configurations: a short fault embedded inside a large plate; a normal fault that becomes steeper with depth ('anti-listric' inclination); and a long strike-slip fault above a faulted rigid basement. The slip and drag along these faults are examined with analytical and numerical models and the results are compared with some laboratory experiments.

2. Drag along a short fault

The development of fault drag reflects the nonuniform deformation in close proximity to a fault. In this section we examine the deformation field for a short fault embedded within a large plate.

We first consider an unfaulted plate that deforms uniformly into a rhomb-shape body under simple shear γ_x parallel to the X-axis (Fig. 2A). The original vertical line AA′ in the center of this

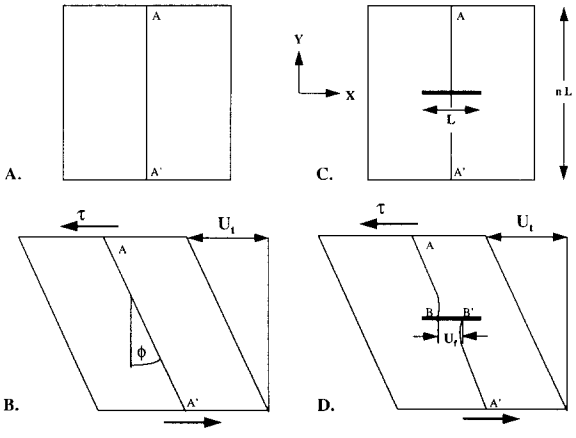

Fig. 2. Deformation and displacements within a faulted plate under plane-strain conditions. (A) Undeformed, homogeneous plate. (B) The original plate of A is deformed by simple shear $\gamma_x = \tan \phi_x$; the displacement of the top of the plate with respect to its base is $U_t = nL \tan \phi_x$; the original line AA' is deformed by simple shear. (C) An undeformed plate of dimensions nL with a fault of length L in its center (solid heavy line). (D) The original plate of C deformed by simple shear $\gamma_x = \tan \phi_x$; the internal deformation of the plate is accommodated by slip along the fault and by continuous, nonuniform deformation away from the fault; the original line AA' is deformed into the line $ABB'A'$ in which the segment BB' is the slip along the fault U_f.

plate rotates by an angle ϕ, where $\phi = \arctan \gamma_x$ (Fig. 2B). Consider now the deformation of a similar plate that includes a fault of length L emplaced in its center (Fig. 2C). In the faulted plate the applied deformation γ_x is accommodated by both continuous deformation within the plate and by slip along the fault (Fig. 2D). The original line AA′ of Fig. 2A is now deformed into a discontinuous line ABB′A′ in which AB and B′A′ are curved lines and the segment BB′ equals the slip along the fault U_f (Fig. 2D). The line segments AB and B′A′ in Fig. 2D are *concave* in the direction of slip, namely, this fault displays reverse drag. The drag *must* be reverse because the plate is deformable and because the fault is shorter than the plate.

To quantify the above process we consider the deformation of an elastic square plate which is isotropic and subjected to plane-strain deformation. The length of the fault within the plate is L and the plate dimensions are $n \cdot L$ by $n \cdot L$ (Fig. 2C). The simple shear strain is $\gamma_x = \partial U/\partial y$, where U is the displacement in the X-direction. The strain ϵ_{12} is:

$$\epsilon_{12} = \tfrac{1}{2}(\partial U/\partial y + \partial V/\partial x) = \tfrac{1}{2}\gamma_x$$

where V is the displacement in the Y-direction. The shear stress τ associated with the strain ϵ_{12} in an elastic plate is:

$$\tau = 2G\epsilon_{12} = G\gamma_x \qquad (1)$$

where G is the elastic shear modulus. The line AA′ deforms and the total displacement, U_t, of A with respect to A′ is (Fig. 2B):

$$U_t = nL\tan\phi_x = nL\gamma_x = nL(\tau/G) \qquad (2)$$

When the plate includes a fault, U_t is accommodated by continuous displacement within the medium, and by slip along the fault, U_f (Fig. 2D). The analysis of a crack subjected to mode II loading in an elastic solid (e.g., Lawn and Wilshaw, 1975) indicates that the displacement at the center of a frictionless fault of length L is:

$$U_f = (1-\nu)L(\tau/G) \qquad (3)$$

This equation indicates that the resistance to slip along a fault is not only frictional, but also includes a contribution from the resistance of the medium to slip along the fault.

Equation (3) is divided by Eq. (2) to compare the displacement along the fault U_f with the total displacement U_t:

$$U_f/U_t = (1-\nu)/n \qquad (4)$$

This equation indicates that the slip along the fault is only a fraction of the total deformation of the plate. The relative amount of slip along the fault is proportional to the ratio between the fault length, L, and the dimensions of the plate, nL. Further, the amount of slip does not depend on the shear modulus of the plate or the intensity of the shear stress, because both the slip along the fault (Eq. 3) and the continuous deformation of the plate (Eq. 2) are proportional to the same ratio of τ/G. Thus, changing τ or G (by selecting a stiffer or a more compliant material) does not affect the ratio U_f/U_t.

The above derivations are for a frictionless fault embedded in a linear, elastic solid. However, as the resistance to fault slip (Eq. 3) and the resistance to continuous deformation of the host medium (Eq. 2), are proportional to the same rheological parameters (τ/G for an elastic solid), it is possible that Eq. (4) has similar character for other rheologies (see Discussion).

3. Numerical modeling of fault drag

3.1. Drag along a short fault

The analytical solution above is restricted to a nonfrictional fault embedded in a linear, elastic solid. We now present numerical solutions for more realistic cases in which the frictional fault is embedded in an elastic–plastic solid. The numerical calculations were conducted with the finite-element program ABAQUS. Details of the models and the rheological parameters appear in the Appendix.

The first model, marked SHORT1, consists of an elastic–plastic plate under plane-strain conditions with one fault parallel to the X-axis. This model is a square plate of 1 m by 1 m with a central fault of length $L = 0.5$ m and friction coefficient

of $\mu = 0.5$ (Appendix). This model was loaded by remote stresses (Appendix) of $\sigma_1 = 150$ MPa, $\sigma_3 = 8$ MPa; σ_1 is oriented at 50° with respect to the fault (Fig. 3). The associated remote strain (Appendix) is maximum shortening of 0.13, maximum extension of −0.12, and the maximum shortening is 47° from the fault (shortening is positive). The deformed model is shown in Fig. 3A without displacement exaggeration; details of the fault termination are shown in Fig. 3B.

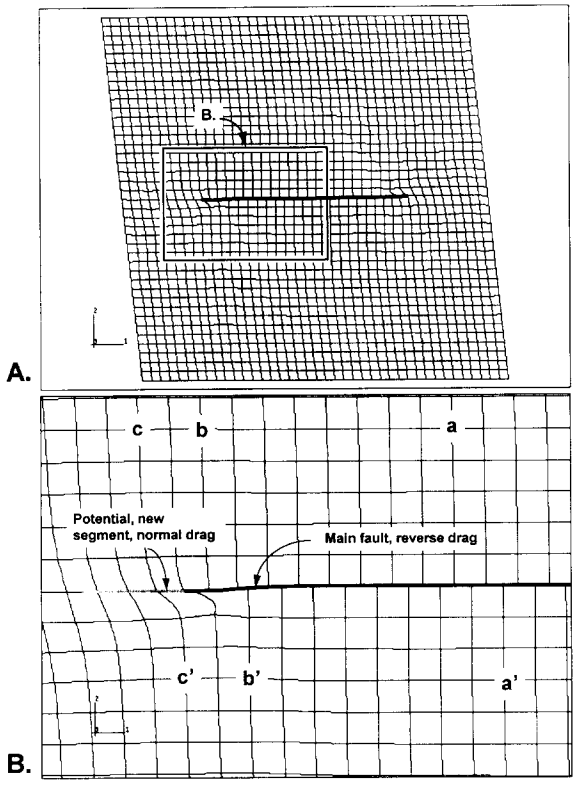

Fig. 3. Finite-element solution for the deformation of a faulted plate under plane-strain conditions (model SHORT1 – see the Appendix for details). This solution is for a 1×1 m plate with 1600 elements and a 0.5-m-long strike-slip fault at its center (solid, heavy line in A). The plate has an elastic-plastic rheology with strain hardening and the friction coefficient of the fault is 0.5. The original, undeformed shape of the model is square; the plotted thin lines formed an orthogonal grid of equally spaced lines before the deformation. (A) The model deformed under maximum shortening of 0.13, maximum extension of −0.12 (shortening is positive), and maximum shortening is 47° from the fault (see the Appendix and Fig. 13A for the boundary conditions). (B) Detail of the model in A. Note the variations in drag along the fault: reverse drag along the central part of the main fault (line *aa'*) and normal drag close to its termination (line *bb'*) and close to the potential extension (line cc').

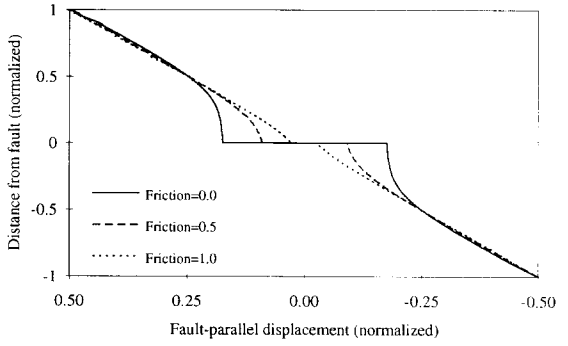

Fig. 4. Fault-parallel displacement along a line normal to the fault and at its center (line ABB'A' in Fig. 2D). Results of finite-element calculations for model SHORT1 with friction coefficients of 0.0, 0.5 and 1.0 (see Fig. 3 and the Appendix for details). The models were deformed by the same remote strain that is shown in Fig. 3. The fault-parallel displacement is shown as fraction of the total displacement, U_t, and the distance from the fault center as a fraction of fault length, y/L.

The calculations of SHORT1 were repeated with the above loading for fault friction values of 0.0, 0.5 and 1.0. The calculated displacement profiles (lines AB and A'B' of Fig. 2D) for the different friction values are presented in Fig. 4. These curves indicate that larger friction corresponds, as expected, to smaller slip along the fault. These displacement profiles also display reverse drag similar to that suggested qualitatively in Fig. 2 and shown in Fig. 3 for friction of 0.5. Further, the intensity of the drag is largest for the solution with zero friction. The drag along the fault is noticeable to a distance of 0.5 L from the fault (Fig. 4), and at larger distances no drag is apparent. Figure 4 also indicates that the slip along the fault is a fraction of the total displacement. The displacement ratio in the numerical solution for a fault with zero friction is $U_f/U_t = 0.35$. The displacement derived from Eq. (4) for an elastic plate with $1/n = 0.5$ and $\nu = 0.25$, is $U_f/U_t = 0.32$. The displacement along the fault in the numerical experiment is larger than the fault displacement in the elastic solution (Eq. 4), because the elastic–plastic rheology of the model permits

larger slip along the fault. The additional slip is accommodated by local, intense deformation close to the fault termination zones.

The numerical models show that the sense of drag and its intensity may vary along the fault. Figure 3B is a map of the calculated deformation at the proximity of the fault in model SHORT1. The reverse drag at the center of the fault (line aa′ in Fig. 3B) decreases in intensity toward the termination zone of the fault, and line bb′ in Fig. 3B already displays slight normal drag. If the fault were to propagate along its trend (gray line marked 'Potential, new segment' in Fig. 3B), the new segment would display normal drag.

The variations in the sense of drag and its magnitude are more clearly presented in another model, SHORT2 (Appendix). In this model the plate is 100 m by 10 m and the fault is 1 m long; the elements become smaller toward the termination zones of the fault (Fig. 5A). This model was subjected to remote stresses of $\sigma_1 = 64$ MPa and $\sigma_3 = -44$ MPa (tensile); σ_1 is oriented at 50° with respect to the fault. The associated remote strain is maximum shortening of 0.021 and maximum extension of −0.019 maximum shortening is 46.5° from the fault.

The change in the sense of drag is apparent here by comparing line aa′ in the central part of the fault with line bb′ close to the termination zone (Fig. 5B). Line aa′ displays the largest reverse drag, whereas line bb′ displays normal drag. Similar variations of the drag were observed in several laboratory models discussed later.

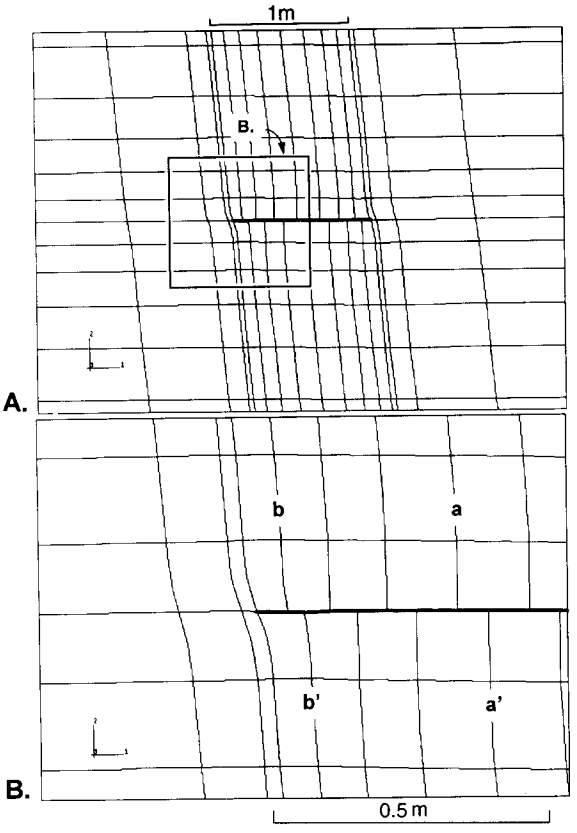

Fig. 5. Finite-element solution for the deformation of a short fault in a large plate (model SHORT2, see the Appendix for details). This is a plane-strain model of 100 m long and 10 m wide with 1-m-long fault at its center (Fig. 13B). The plate is of elastic-plastic rheology with strain hardening and the fault is with friction of 0.1. (A) Close up of the fault area as deformed under a remote strain with maximum shortening of 0.021 and maximum extension of −0.019 (shortening is positive); maximum shortening is 46.5° from the fault. Solid, heavy line is the central fault; the thin lines formed a rectangular grid before the deformation. (B) Detail of the model in A. Note the variations in drag along the fault: reverse drag along the central part of the main fault (line aa′) and normal drag close to its termination and potential extension (line bb′).

3.2. Drag along a curved normal fault

Probably the better known cases of reverse drag are associated with normal faults. Hamblin (1965) presented an extensive review of several mechanisms for reverse drag along normal faults; he included multiple stages of deformation, elastic rebound, sagging, inversion of slip directions and differential compaction. Hamblin presented many examples of reverse drag from normal faults on the Colorado Plateau and elsewhere, and he concluded "that reverse drag develops from some fundamental mechanism associated with normal faulting." (Hamblin, 1965, p. 1161). He then attributed the reverse drag to the decrease of the fault inclination with depth (such as in listric geometry) (Fig. 1B). Under this geometry, a void opens at the surface into which the hanging wall collapses forming reverse drag and roll-over structures. This approach has been adopted by many (e.g., Bruce, 1972; Davis, 1984).

We studied the drag along a curved normal

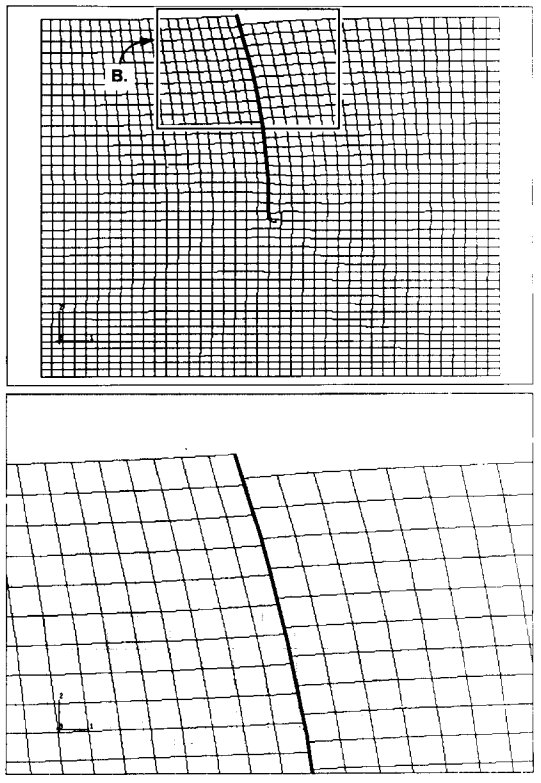

Fig. 6. Finite-element solution for the deformation associated with a normal fault (model NORMAL1, Appendix I). The figure displays a vertical section normal to the strike of the fault for plane-strain conditions. The undeformed model is 8 km by 8 km with 1600 elements; its rheology is elastic-plastic with strain hardening. The fault steepens with depth from 75° at the surface to 90° at depth of 4 km where it terminates; the fault friction is 0.5. (A) The deformed model after horizontal extension of $\epsilon_x = 0.0125$ under loading by gravity and vertical load of 13 MPa at the surface (Fig. 13C and the Appendix). The displacements are shown without exaggeration. (B) Details of the upper part of the fault in A; faint lines are the undeformed mesh. Note the reverse drag of the solid, deformed lines.

fault by numerical modelling of a fault that becomes steeper with depth ('anti-listric') (Fig. 6). The deformation was calculated in a vertical cross-section normal to the strike of the fault under plane-strain conditions (see model NORMAL in the Appendix). The calculations are for a region of 8 km by 8 km with a 4 km deep fault at the center of the model (Fig. 6). The fault dips 75° at the ground surface and it steepens monotonously to 90° at 4 km. The medium is of elastic–plastic rheology and bulk density of $\rho = 2600$ kg/m^3 (Appendix). The model of Fig. 6 was extended horizontally by 2.5% (in the X-direction) and under the effect of gravity and overburden. Accordingly, the boundary displacements were $U_x = \pm 100$ m at $X = \pm 4$ km, $U_y = 0$ at $Y = -4$ km, and $Y = 4$ km is a free surface.

Figure 6 is the distorted shape of the model due to the lateral extension and the weight of the rocks; the fault has friction of 0.5. This figure shows the deflection of initially horizontal lines that are now curved at the proximity of the fault in a reverse drag style. These results for an anti-listric fault indicates that reverse drag and rollover can form under conditions of a normal fault that steepens with depth. In other words, reverse drag is not an indication for listric geometry.

The drag associated with the normal fault of Fig. 6 is generally similar to the drag of the strike-slip fault in Fig. 3. The reverse drag that prevails in both these cases reflects the finite length of these faults as indicated in equation (4) and its associated discussion (see above).

4. Discussion

4.1. Comparison with laboratory models

The experimental works of Freund (1974) and Odonne (1990) display some drag features along short faults. Freund (1974) deformed cakes of plasticene cut by 5 faults oriented 15°, 30° or 45° with respect to the axis of maximum shortening; the experiment with 30° faults is displayed in Fig. 7A. Freund was careful to enclose both ends of each fault inside the plasticene cake. The cake accommodated the deformation by continuous deformation of the plasticene and slip along the faults (Fig. 7B for shortening of $\epsilon_x = -\epsilon_y = -0.5$). The initially planar faults were distorted into sigmoidal shapes as part of this deformation, and zones of normal and reverse drag appeared in the experiments (marked by N and R, respectively, in Fig. 7B). However, the existence of several faults in these experiments prohibits a simple quantitative comparison with the present analysis of a short, isolated fault.

The experiments of Odonne (1990) provide a more tractable configuration. He used large plates of wax, 70 cm by 45 cm and 1.1 cm thick that were deformed by in-plane compression. The plates were shortened in the Y-direction by two rigid bars while permitting unconstrained deformation in the X-direction (Fig. 8A). We discuss here one of Odonne's experiments in which a 28 cm long fault was cut into the center of the plate at an angle of 30° with respect to the Y-axis (Fig. 8A). The displacements within the plate were carefully mapped by Odonne (1990) (Fig. 8B).

Some features of the displacement field in Odonne's experiments closely resemble the present predictions of fault drag. First, reverse drag dominates the distortion of the marker lines which were originally at 30° and 60° with respect to the fault (compare Fig. 8A with Figs. 3, 4). Second, the slip along the fault, U_f, is only a fraction of the remote displacement, U_t (Fig. 9). Figure 9 is a plot of the fault-parallel displacements along profile cc′ (Fig. 8B) normal to the fault (solid

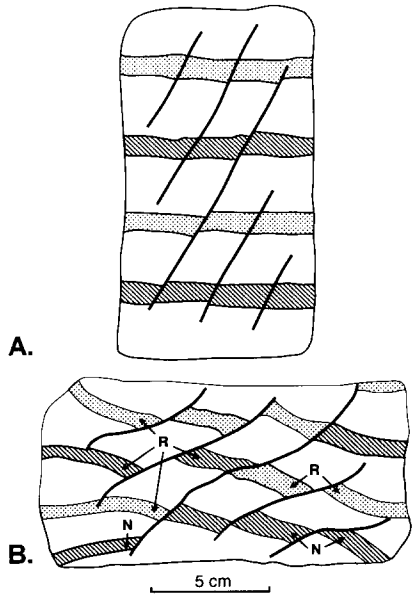

Fig. 7. Deformation of a faulted plasticene cake within a rigid deformation apparatus (after Freund, 1974). The cake was deformed under plane-strain conditions and the faults were precut into the plasticene. (A) Undeformed plate with five faults inclined 30° with respect to the shortening direction (Y-axis). The four horizontal zones with dots and diagonal patterns are passive lines marked on the plasticene. (B) The plate of A after vertical shortening of $\epsilon_y = 0.5$ and horizontal extension of $\epsilon_x = -0.5$. The passive lines are displaced along the faults and deformed inside the blocks bounded by the faults. One can note that in the areas marked by the letter R, the passive lines are bent with *concave* side toward the slip direction, thus indicating reverse drag. In other areas marked by the letter N, the passive lines are bent with *convex* side toward the slip direction, thus indicating normal drag.

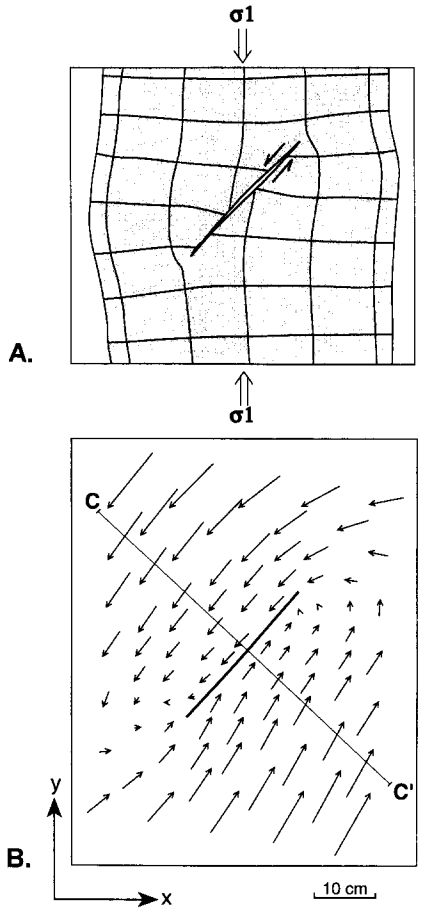

Fig. 8. Deformation of a faulted wax plate under uniaxial compression in the Y-direction (after Odonne, 1990). The plate is 1.1 cm thick and it includes one fault originally inclined at 30° with respect to the shortening direction; the grid of thin lines was originally rectangular and equally spaced in the X and Y directions making angles of 30° and 60° with respect to the fault. (A) The plate after shortening of $\epsilon_y = -0.2$ (after fig. 3a of Odonne, 1990). Note the reverse drag at the central part of the fault and the normal drag close to the termination zones. (B) The measured displacement vectors relative to the center of the fault after removal of the fault rotation (after fig. 6 of Odonne, 1990).

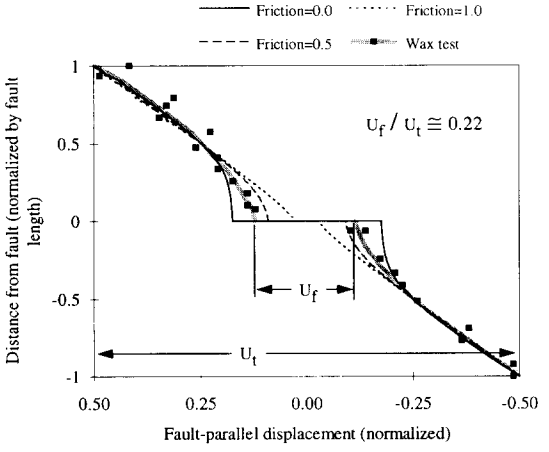

Fig. 9. Measured fault-parallel displacement along the line cc' (Fig. 7B) in the wax experiment of Odonne (1990). The displacements measured by Odonne on both sides of the cc' line and to a distance of 5 cm away, were projected to the line. The measured displacements (solid squares) are normalized with respect to the maximum displacement away from the fault, U_t, and they are plotted at distances normalized by the length of the fault, L; a thick, gray line within the cloud of the solid squares is our estimate of the continuous distribution of the displacement in this experiment. The results of the finite-element calculations of Fig. 4 are also plotted, and the experimental data points fall between the curves for friction coefficients of 0.0 and 0.5.

squares); the figure also includes our estimate of the quasi-continuous distribution of the displacement in the experiment (thick, curved line), and the displacement profiles calculated in model SHORT1 (after Fig. 4). The experimental profile indicates that $U_f/U_t \approx 0.22$ (Fig. 9), namely the slip along the fault is only a fraction of the total displacement as predicted in the analytical model (Fig. 2). The distribution of the displacement in the experiments (solid squares and thin curved line in Fig. 9), is similar in character to the displacement profiles calculated numerically for a finite fault in an elastic–plastic model (dashed lines in Fig. 9). The experimental displacements appear to fall between the predicted lines for friction of 0.0 and 0.5, indicating friction of about 0.25.

Doblas (1990) conducted experiments to examine the shear at the interface between two wax blocks of contrasting competence. In Doblas' experiments, a block of competent wax was emplaced inside a plate of less competent wax and the entire plate was subjected to pure shear. Maximum compression was oriented 45° with respect to the contact between the two wax blocks and large slip occurred along this contact. The block of the more competent wax acted as a complicated fault zone of finite length. Doblas' experiments "display anomalous apparent drag effects" (Doblas, 1990, p. 30), as well as variations of the sense of drag along the fault; these results are in good agreement with the predictions of the present model.

The rheological properties of the wax (nonlinear viscous) in the experiments of Odonne (1990) and Doblas (1990) differ from those of the solids in the above numerical solutions (nonlinear elastic–plastic) and the above analytical solution (linear elastic). We therefore think that the observed similarity in the character of the displacement distribution supports the argument made above with regard to Eq. (4). It suggests that the displacement field associated with a short fault reflects the geometry of the fault (finite length) and the boundary loading (displacement applied away from the fault), and this displacement field does not depend on the specific rheology of the medium.

In conclusion, the above analyses and experiments show that: (1) reverse drag is an essential feature for slip along short faults; (2) the remote displacement is related to the slip on the fault by a simple geometric criterion of Eq. (4); and (3) the magnitude of the drag and the sense of the drag (normal or reverse) may vary along a given fault.

4.2. Drag along a long fault

Figure 10 is a schematic view of a typical experiment of a long strike-slip fault (e.g., Richard et al., 1991). This type of experiment includes at least two layers. The lower layer is built of stiff blocks (usually metal or wood) separated by a vertical fault; this layer represents an igneous basement or stiff upper mantle. The upper layer is usually made of clay, silicon putty or sand that represents the deformable sedimentary cover or the crust.

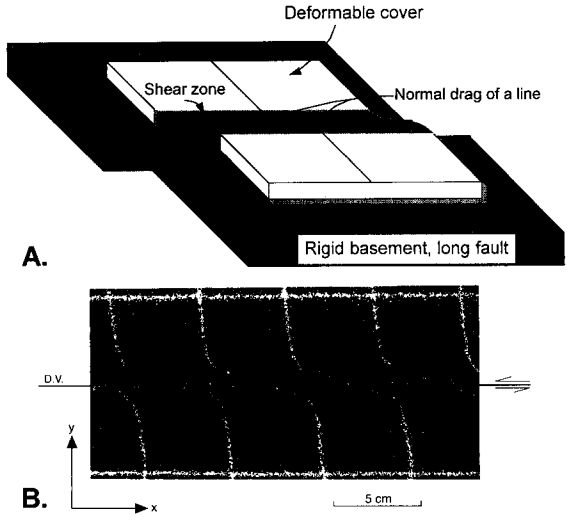

Fig. 10. An experimental setup for a long strike-slip fault above a basement (modified after Richard and Kranz, 1991). (A) A deformable layer is emplaced on a two rigid blocks that are displaced horizontally with respect to each other. A shear zone forms above the basement fault and it is eventually cut by a master fault. (B) A view of the top surface of an experiment by Richard et al. (1991) with the setup of A. The total displacement along the basement fault (D.V.) was 8 cm; white lines originally normal to the fault display normal drag due to the shear deformation prior to the slip along the master fault.

As the two basement blocks are perfectly rigid, the slip along the basement fault equals the total displacement between the blocks, U_t. In the upper layer, the displacement away from the fault is also U_t as the two layers are bonded, and a wide shear zone develops in the upper layer above the basement fault (Fig. 10A) (Groshong and Rodgers, 1978; Sylvester, 1988; Richard et al., 1991; Richard and Kranz, 1991). The predominant deformation in the shear zone is simple shear parallel to the displacement direction of the lower blocks. The dimensions of this zone and the nature of its structural features depend on the geometry of the deformation apparatus and the rheology of the experimental materials. Within the shear zone, the displacement is accommodated by both continuous shear and slip along the fault, U_f. In general $U_f < U_t$, and the displacement difference $U_t - U_f$ is accommodated by continuous deformation in the shear zone. Lines and layers within the shear zone deform to become *convex* toward the direction of slip, namely they become compatible with normal drag (Fig. 10).

Eventually, a few faults in the central part of the shear zone link to each other and form a master fault that coincides with the basement fault (Fig. 10B). Subsequent displacement along the basement fault is accommodated by slip along the master fault and the curved lines display an apparent normal drag. However, this apparent drag formed *before* the development of the master fault. Thus according to the model the drag is the result of a previous deformation stage and it is not related to the slip along the fault or to its frictional resistance. This conclusion is the same as the statement of Dennis (1972) cited in the Introduction.

5. Conclusions

The above analysis leads to the following deductions:

(A) *Slip along a fault of finite length*

(1) The displacement U_f along a fault of finite length is only a fraction of the total displacement U_t accommodated by the host body.

(2) The ratio of U_f/U_t depends primarily on the fault length and the boundary loading, and this ratio only slightly depends on the body rheology. For an elastic body:

$$U_f/U_t = (1 - \nu)/n$$

This equation is generally valid for the tested cases of elastic–plastic solid with strain hardening (numerical solutions) and for a viscous body (wax experiments).

(B) *Fault drag*

(1) The sense of drag along a finite fault must be reverse at the center part of the fault. The drag also varies from reverse drag at the fault center to normal drag at the termination of the fault.

(2) Normal drag develops along long faults and faults that are associated with the motion of rigid blocks. This drag most likely represents the pre-

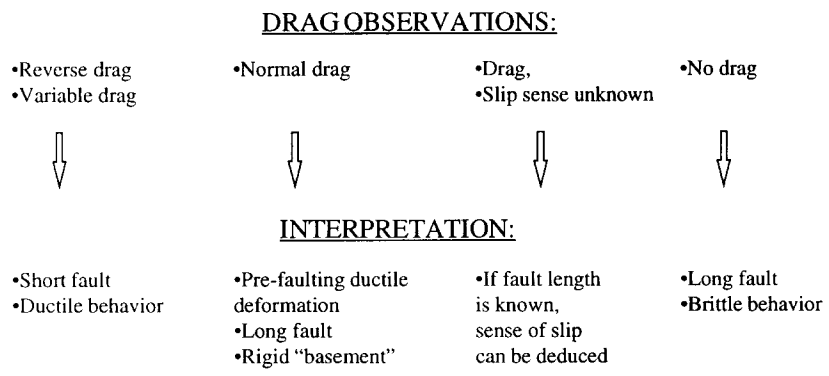

Fig. 11. A scheme for the analysis of fault 'drag' features according to the present study. The four groups of field or experimental observations of the upper row correspond to the interpretation lower row.

faulting deformation rather than frictional resistance (see Dennis, 1972, p. 302).

(3) Reverse drag may develop along normal faults that steepen with depth (anti-listric). This reverse drag reflects the finite length of the fault. Reverse drag may also develop along normal faults with listric geometry in mechanisms proposed by Hamblin (1965).

(C) *Applications*

(1) Similarly to previous studies (e.g., Hamblin, 1965), we conclude that there is no rule-of-thumb for fault drag.

(2) Figure 11 is a proposed scheme for the interpretation of fault drag. This figure is based on the cases considered in the present analysis (strike-slip and normal faults embedded in mechanically uniform medium). Figure 11 leads from four groups of field or laboratory observations to the most likely interpretation.

Acknowledgements

The discussions and comments of Lou Boldt, Martin Pruatt and Zvi Garfunkel contributed to the study. The reviews and comments by F. Odonne and W. Power improved an earlier version of the manuscript. The study was supported by Kerr-McGee fund, School of Geology and Geophysics, University of Oklahoma.

Table 1
The properties of the numerical models in the present analysis

Model name	Size, fault length	Elements (number, type)		Matrix rheology (elastic parameters) (plastic parameters) (density)	Friction range	Boundary conditions and loads
		Matrix	Fault			
SHORT1	1×1 m, 0.5 m	1600, CPE8R	19, ISL22	$E = 10^{10}$ MPa, $\nu = 0.25$ $\sigma_0 = 10^8$ MPa, $n = 10$	0.0–1.0	Plane-strain displacements in Fig. 13A
SHORT2	100×10 m, 1.0 m	443, CPE8R	8, INTER3	$E = 10^{10}$ MPa, $\nu = 0.25$ $\sigma_0 = 10^8$ MPa, $n = 10$	0.0–1.0	Plane-strain, displacements in Fig. 13B
NORMAL1	8×8 km, 4 km	1600 CPE8	20, INTER3	$E = 5 \cdot 10^8$ MPa, $\nu = 0.25$ $\sigma_0 = 6.5 \cdot 10^7$MPa, $n = 10$ $\rho = 2600$ kg m^{-3}	0.0–0.5	Plane-strain, displacements in Fig. 13C

Appendix

The numerical calculations were conducted with the finite-element code ABAQUS. This code is capable of mechanical analysis of two- and three-dimensional models with large and nonlinear deformation. The code features a large element library with linear and nonlinear material properties, time-stepping algorithms and solution techniques for solving problems with nonlinear rheology. The ABAQUS code was developed by HKS Inc., Pawtucket, Rhode Island.

In the present study we explored a wide range of models with various geometries and rheological properties. The properties of the three models presented here are listed in Table 1. Models SHORT1 and SHORT2 were for plane-strain deformation of a plate with nonlinear elements (ABAQUS type CPE8R or CPE8) for the continuous medium, and nonlinear interface elements for the fault zone (ABAQUS type SLIDE LINE and INTER3). The medium is a three-parameter elastic–plastic solid with strain hardening. It was defined by using a Ramberg–Osgood flow law of the form:

$$\epsilon = (\sigma/E)\left[1 + (\sigma/\sigma_0)^{n-1}\right]$$

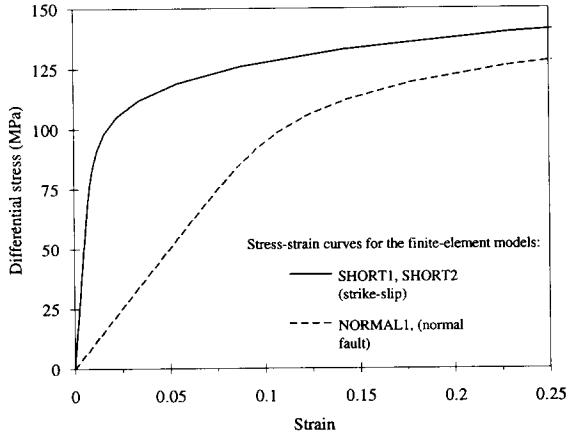

Fig. 12. Rheology of the material used for the numerical models. These stress-strain curves were calculated by using the Ramberg–Osgood equation of the Appendix and the parameters listed in Table 1.

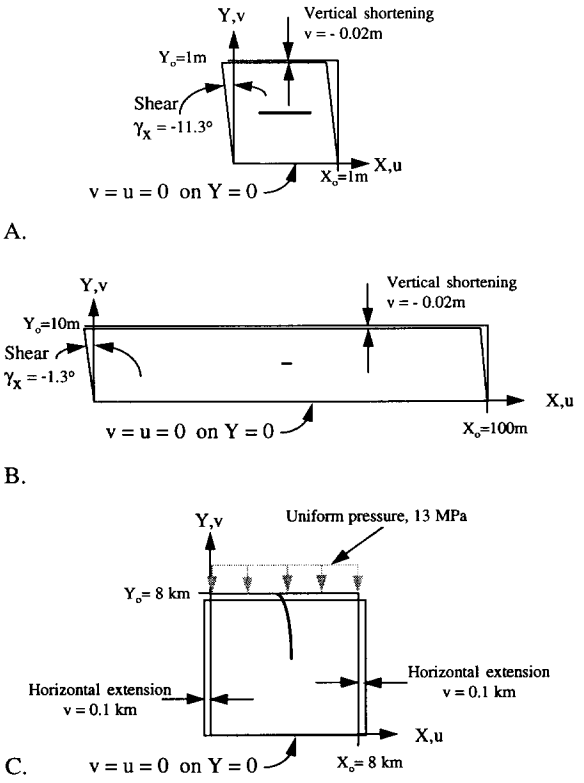

Fig. 13. Boundary conditions of the three models. Heavy line in the center of each model indicates the emplaced fault; the models deformed under plane-strain conditions. Note the scale difference between the models (see Table 1 for models' properties). (A) Model SHORT1 with its displacement boundary conditions. (B) Model SHORT2 with its displacement boundary conditions. (C) Model NORMAL1 with its displacement boundary conditions (base and both sides) and stress boundary conditions (top).

where ϵ and σ are the uniaxial strain and stress, E is Young modulus, σ_0 and n are material parameters that characterize its plastic behavior. The selected parameter values are listed in Table 1 and the corresponding stress-strain curves appear in Fig. 12 for the three models.

The models were loaded by displacements or pressures along their boundaries. For sake of numerical convenience the boundary loading were defined in terms of the coordinate system of the models, namely shortening and shear are defined as parallel or perpendicular to the coordinate

axes of the models (Fig. 13). These boundary loads generated relatively uniform stress and strain fields away from the embedded fault. In the text we refer to these fields as the *remote stress* and the *remote strain* fields. The remote fields are given in terms of principal stress and strain axes and their orientations are specified with respect to the orientation of the central fault. The fields of the remote stress and the remote strain are perturbed at the proximity of the embedded faults due to its slip. The three models were subjected to different boundary loads. Models SHORT1 and SHORT2 were subjected to vertical shortening v, and simple shear γ_x, along their boundaries as are shown in Fig. 13A and 13B; these boundaries were enforced to move by the amounts and in the directions shown. The fault normal shortening v, was applied first, and the simple shear γ_x was applied later. Model NORMAL1 was subjected to horizontal extension u, on both sides, and to a uniform pressure of 13 MPa on the upper surface (Fig. 13C); this uniform pressure represents the overburden load of 0.5 km. The gravity load was applied first, vertical pressure was applied second and horizontal extension was applied third. The stress, strain and displacement fields inside the models were computed by the program.

The calculated displacement fields for models SHORT1 and SHORT2 are only slightly affected by the actual parameter values. For model NORMAL1 of the normal fault calculations, we selected a fairly weak material to allow the medium to deform under its own weight; otherwise a mode I opening of the fault would have occurred.

References

Billings, M.P., 1972. Structural Geology, 3rd ed. Prentice-Hall, Englewood Cliffs, NJ, 606 pp.

Bruce, C.H., 1972, Pressured shale and related sediment deformation; mechanism for development of regional contemporaneous faults. Am. Assoc. Pet. Geol. Bull., 57: 878–886.

Davis, G.H., 1984. Structural Geology of Rocks and Regions. John Wiley and Sons, New York, NY, 592 pp.

Dennis, J., 1972. Structural Geology. John Wiley, New York, NY, 532 pp.

Doblas, M., 1990. Efecto de arrastre aparente en zonas de cizalla: resultados de un modelo experimental. Geogaceta, 8: 30–32 (in Spanish with English abstract).

Freund, R., 1974. Kinematics of transform and transcurrent faults. Tectonophysics, 21: 93–134.

Groshong, R.H. and Rodgers, D.A., 1978. Left-lateral strike slip fault model. In: J.S. Wickham and R.E. Denison (Editors), Structural Style of the Arbuckle Region. Geol. Soc. Am., South Central Sect., 1: 2–7.

Hamblin, W.K., 1965. Origin of "reverse drag" on the downthrown side of normal faults. Geol. Soc. Am. Bull., 76: 1145–1164.

Hills, E.S., 1963. Elements of Structural Geology. Methuen and Co., London, 483 pp.

Johnson, A.M., 1970. Physical Processes in Geology. Freeman, Cooper and Co., San Francisco, CA, 577 pp.

Lawn, B.R. and Wilshaw, T.R., 1975. Fracture of Brittle Solids. Cambridge University Press, London, 204 pp.

Odonne, F., 1990. The control of deformation intensity around fault: Natural and experimental examples. J. Struct. Geol., 12: 911–921.

Richard, P. and Kranz, R.W., 1991. Experiments on fault reactivation in strike slip mode. Tectonophysics, 188: 117–131.

Richard P., Mocyuent, B. and Cobbold, P.R., 1991. Experiments on simultaneous faulting and folding above basement wrench fault. Tectonophysics, 188: 133–141.

Sylvester, A.G., 1988. Strike-slip faults. Geol. Soc. Am. Bull., 100: 1666–1703.